

# Effects of blade flexural rigidity on drag force and mass transfer rates in model blades

Jeffrey T. Rominger\* and Heidi M. Nepf

Department of Civil and Environmental Engineering, Massachusetts Institute of Technology, Cambridge, Massachusetts

## Abstract

We created a model physical system to investigate the role of blade rigidity in setting forces and rates of mass exchange for a blade exposed to unsteady flow in a vortex street. Using a combination of experimental and theoretical investigations, we find that, broadly, both the forces and the mass exchange are higher for more flexible blades. Below a critical value of the dimensionless blade rigidity, inertial forces from the rapidly deforming blades become significant, increasing both the time-averaged and instantaneous forces on the blade. Mass transfer is also affected by blade rigidity. As blades deform, they alter the relative fluid motion at the blade surface, affecting mass fluxes. We developed a novel experimental method that simulates nutrient uptake to a blade using the transport of a tracer compound into polyethylene models. Through these experiments and modeling, we demonstrate that increased blade flexibility is associated with increased mass transfer to blades.

Kelp blades alter their morphology via the process of phenotypic plasticity, which is the process through which the manifested traits of an organism adapt to changes in environmental stimuli, such as changes in light or nutrient availability, changes in mechanical stresses, changes in temperature, and so forth. In kelp blades, the length, width, and thickness of the blades, as well as the overall characteristics of the shape (e.g., rectangular, tapered, undulatory, etc.) can change over the timescale of the kelp life cycle in response to hydrodynamic conditions (Druehl and Kemp 1982; Koehl et al. 2008). For kelp, two of the most important environmental constraints on blade development are nutrient flux and hydrodynamic drag. Blades must acquire nutrients directly from the surrounding water. Furthermore, in the coastal ocean, kelp blades can be exposed to strong currents and waves that can break blades or dislodge entire fronds from the substrate. For this reason, documented observations of kelp blade morphology are traditionally grouped into two categories: “exposed” and “sheltered,” which describe the blades’ general exposure to rapid flow and high drag forces from waves and currents, and to slow flow and reduced drag forces, respectively (Koehl et al. 2008).

In sheltered environments, some blades have undulations, or ruffles, along the flow-parallel edges (Koehl and Alberte 1988; Koehl et al. 2008), and this morphology, which can promote flapping, has been suggested to increase flux at the blade surface at the expense of also increasing drag forces (Koehl and Alberte 1988). In sheltered environments, however, drag forces are generally lower and may not be an important factor. In the same study, the morphologies observed at exposed sites (e.g., thicker, narrower, more strap-like blades) exhibited both less flapping and lower drag forces per unit blade area. Gerard and Mann (1979) also observed clear differences in blade thickness between flow-exposed and flow-sheltered sites in *Laminaria longicuris*. The thickness of the flow-exposed blades was more than three times the thickness of the flow-sheltered blades. The trend of thicker blades at exposed

sites has also been documented in the following macroalgae genera: *Agarum* (Duggins et al. 2003), *Durvillaea* (Cheshire and Hallam 1989), *Ecklonia* (Wernberg and Thomsen 2005), *Eisenia* (Roberson and Coyer 2004), *Gigartina* (Jackelman and Bolton 1990), *Laminaria* (Parke 1948; Sjøtun and Frederiksen 1995; Duggins et al. 2003), *Macrocystis* (Hurd et al. 1996), and *Pachydictyon* (Haring and Carpenter 2007). Moreover, the same behavior has been observed in seagrass blades of various species (Peralta et al. 2006).

Changes in blade thickness ( $h$ ) can have significant effects on the mechanical properties of the blade. The blade stiffness in tension is directly proportional to the blade cross-sectional area, and thus is linearly proportional to blade thickness. However, for a blade with a nominally rectangular cross section, the bending rigidity is proportional to the cube of the blade thickness. Thus, changes in thickness have a more pronounced effect on the structure’s resistance to bending than its strength under tension. The blades of *Macrocystis* not only have an increased thickness at exposed sites, but they also exhibit longitudinal corrugations (Fig. 1a). These corrugations are fundamentally distinct from the ruffles or undulations observed in species at sheltered sites. The peaks and troughs of the corrugations run parallel to the edges of the blades, whereas undulations or ruffles are oriented perpendicularly to the blade edges (see fig. 1b in Koehl et al. 2008). At flow-sheltered sites, these corrugations are either entirely absent (Hurd and Pilditch 2011) or greatly reduced in amplitude (Hurd et al. 1996). When present, corrugations are regular in amplitude and wavelength, and generally extend almost the full blade length, but at points along the blade individual peaks end, split, or merge with other peaks (Fig. 1b). From previous studies of corrugated materials (Lau 1981; Briassoulis 1986), we propose that the primary function of blade corrugations is to increase blade flexural rigidity. This idea is explored in detail later in the paper. We anticipate from previous studies of flapping flags (Michelin and Smith 2009) that changes in rigidity will affect the degree of blade flapping, which in turn may affect the mean and peak drag on the blade. In addition, based on

\* Corresponding author: jtr@alum.mit.edu

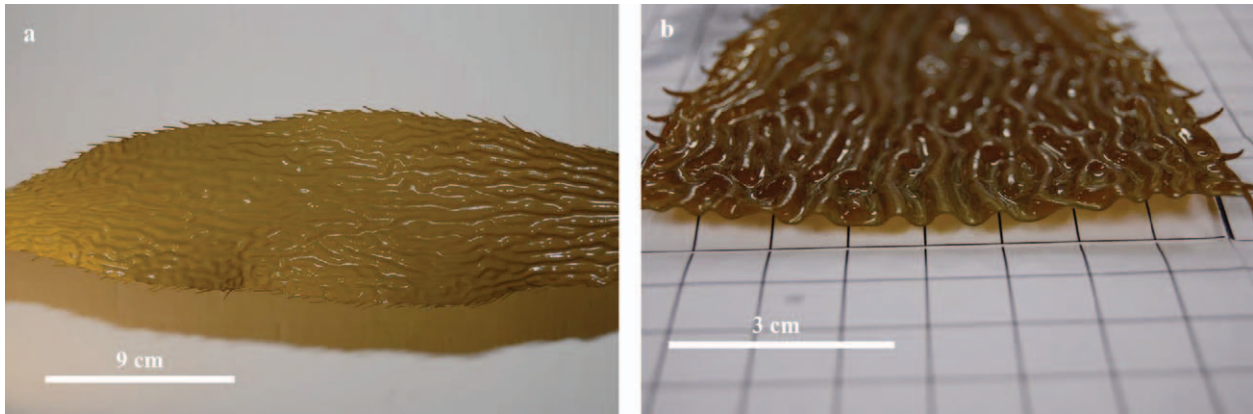


Fig. 1. (a) A photo of a *Macrocyctis* blade, showing the longitudinal corrugations running the full length of the blade. (b) A cut section of a *Macrocyctis* blade, showing the corrugation structure. The cutaway shows the regularity of the corrugation wavelength and amplitude.

previous flux observations (Koehl and Alberte 1988), we anticipate that changes in flapping amplitude may also alter the rate of chemical flux to the blade surface.

When kelp blades can move relative to the flow, the relative fluid velocity at the blade surface and the frequency of the blade motion can affect flux to the blade. Modeling by Stevens and Hurd (1997) and by Stevens et al. (2003) indicated that periodic accelerating flow at the blade surface can greatly enhance flux at the blade surface. Huang et al. (2011) suggested that passive flapping by kelp blades in uniform flow could also enhance nutrient flux. Denny and Roberson (2002) created copper model blades and measured heat flux while mechanically oscillating the blades at different frequencies. They found that increases in blade frequency and increases in the mean flow speed, both of which increase the relative fluid velocity at the blade surface, also both increased scalar flux at the blade surface. There have been many studies of nutrient flux to kelp blades that support the finding that simply increasing fluid velocities increases the rate of mass flux at the blade surface. These studies have used a variety of experimental methods, oftentimes using live kelp blades. Some studies have placed live kelp blades in laboratory flumes and measured rates of  $\text{NO}_3^-$  and  $\text{NH}_4^+$  uptake to blades by monitoring the decrease in nutrient concentration in the flume (Gerard 1982b; Hurd et al. 1996). Koehl and Alberte (1988) placed live blades in a flume to measure carbon uptake rates, which help determine rates of photosynthesis in flow. Hepburn et al. (2007) measured kelp growth rates and tissue nitrogen concentrations in situ to determine the effects of waves on nutrient uptake. In all of these studies, the rate of mass flux increased with increasing fluid velocities, up to the point at which the kelp nutrient requirements were satisfied.

Kelp blades are highly flexible and deform easily in flow. Previous studies of flexible flags in flow (Zhang et al. 2000; Eloy et al. 2008; Manela and Howe 2009) suggest that the flexural rigidity of the kelp blades can control the response of the blade to flow and thus affect the relative fluid velocity at the surface of the blade. In the first part of this study, we investigate the effects of blade flexural rigidity on

the blade drag force. In the second part of this study, we investigate the effects of blade flexural rigidity on mass flux at the blade surface. In our experiments, we deploy flexible model blades of generic morphology in a carefully designed flow field and measure the blade drag force and the rates of mass flux at the blade surface. To measure flux at the blade surface, we develop a novel experimental method for the transfer of an organic compound between the moving water and the model blades. By using model blades rather than live blades, and by retaining control over the structural properties of the model blades, we can precisely vary the flexural rigidity. Ultimately, we seek to explain the documented morphological trends in kelp blades in the context of our experimental drag and flux results.

### Methods

Model blades were placed in a water channel in which  $x$  and  $z$  represented the streamwise and vertical coordinates, respectively (Fig. 2). The blades can be modeled as a slender, inextensible beam of width ( $b$ ), length ( $l$ ), elastic modulus ( $E$ ), density ( $\rho$ ), and second moment of area ( $I$ ). For a rectangular cross section, the second moment of area is

$$I = \frac{bh^3}{12} \tag{1}$$

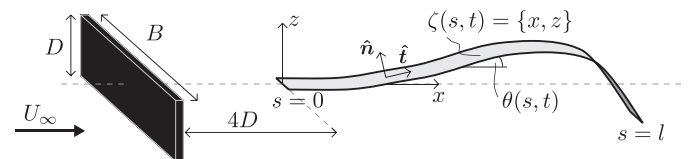


Fig. 2. A flexible blade of length  $l$  in a vortex street created by a bar of height ( $D$ ). The bar spans the flume width ( $B$ ). The blade has width  $b \ll B$ . Blade position is described by  $\zeta = \{x, z\}$ . The fluid velocity upstream of the bar is  $U_\infty$ . The local unit normal and unit tangent vectors ( $\hat{n}$  and  $\hat{t}$ , respectively) are shown at an arbitrary point along the blade.

Table 1. A summary of *Macrocystis* blade morphology observations from Hurd and Pilditch (2011) documenting the measurements of blades from flow-exposed and flow-sheltered sites. The blades at the flow-sheltered sites had no corrugations. The elastic modulus of algal material was reported by Hale (2001).

	Exposed morphology	Sheltered morphology
Blade thickness, $h$ (mm)	0.470	0.425
Elastic modulus, $E$ (Pa)	$5 \times 10^6$	$5 \times 10^6$
Blade length, $l$ (m)	0.62	0.52
Corrugation amplitude, $a$ (mm)	1.37	—
Corrugation wavelength, $\lambda_c$ (mm)	3.08	—
Bending rigidity, $EI$ , formula	$E \frac{a^2 hb}{2} \left( 1 + \frac{\pi^2 a^2}{8(\lambda_c/2)^2} \right)$	$Ebh^3/12$
Bending rigidity/width, $EI/b$ (Pa m <sup>3</sup> )	$4.4 \times 10^{-3}$	$3.2 \times 10^{-5}$

For a corrugated cross section, the second moment of area is approximated by

$$I = \frac{a^2 hb}{2} \left( 1 + \frac{\pi^2 a^2}{8(\lambda_c/2)^2} \right) \quad (2)$$

where ( $a$ ) is the corrugation amplitude and ( $\lambda_c$ ) is the corrugation wavelength (Lau 1981). Importantly, corrugations present a method of increasing bending rigidity that can be accomplished by changing shape, rather than by adding material in order to increase blade thickness.

We define a curvilinear coordinate system in which  $s$  is the distance along the blade,  $\theta$  is the angle formed between the blade and the  $x$ -axis, and  $\zeta = \{x, z\}$  is the blade position vector (Fig. 2). The motion of the blade can be described by the large-amplitude equation of motion for a slender, flexible beam in fluid flow (Alben and Shelley 2008; Michelin et al. 2008):

$$\rho b h \frac{\partial^2}{\partial t^2} \zeta = - \frac{\partial}{\partial s} [EI \theta_{,ss} \hat{\mathbf{n}}] + \frac{\partial}{\partial s} [T \hat{\mathbf{t}}] + F \quad (3)$$

The subscript  $s$  indicates a partial derivative with respect to  $s$ , the distance along the blade. The local unit normal and unit tangent vectors for the blade surface are denoted by the bold symbols,  $\hat{\mathbf{n}} = \{-\sin \theta, \cos \theta\}$  and  $\hat{\mathbf{t}} = \{\cos \theta, \sin \theta\}$ . The acceleration of the blade (the left hand side of Eq. 3), is a function of the fluid forcing ( $F$ ), the internal tension in the blade ( $T$ ), and the blade's resistance to bending (the first term on the right-hand side of Eq. 3). The time coordinate is denoted ( $t$ ). The fluid-forcing term ( $F$ ) describes the complex interactions between the moving fluid and the blade motion. Most simply, this fluid-forcing term includes the combined effects of the fluid drag force, the added mass of the fluid, and the angular acceleration of the fluid as it interacts with the blade curvature (i.e., the Coriolis-type force; Datta and Gottenberg 1975).

We rescale the governing equation using the blade length  $l$  as the characteristic length scale, and the advection timescale,  $l/U_\infty$ , as the characteristic timescale, where  $U_\infty$  is the open channel water velocity, i.e.,  $\hat{s} = s/l$ ,  $\hat{\zeta} = \zeta/l$ , and  $\tau = tU_\infty/l$ . The force terms are scaled with the characteristic hydrodynamic drag,  $\rho_f U_\infty^2 b l$ , with  $\rho_f$  the fluid density. With this scaling, the governing equation in dimensionless

form is

$$\mu \frac{\partial^2}{\partial \tau^2} \hat{\zeta} = - \eta \frac{\partial}{\partial \hat{s}} [\theta_{,ss} \hat{\mathbf{n}}] + \frac{\partial}{\partial \hat{s}} [\hat{T} \hat{\mathbf{t}}] + \hat{F} \quad (4)$$

where  $\hat{F}$  and  $\hat{T}$  are the dimensionless fluid forcing per unit blade length and the dimensionless internal tension in the blade, respectively:

$$\hat{F} = \frac{F}{\rho_f U_\infty^2 b} \quad (5)$$

$$\hat{T} = \frac{T}{\rho_f U_\infty^2 b l} \quad (6)$$

After collecting terms, the dimensionless governing equation reveals two governing parameters:

$$\mu = \rho h / \rho_f l \quad (7)$$

$$\eta = EI / \rho_f b U_\infty^2 l^3 \quad (8)$$

Physically,  $\mu$  represents a ratio of blade inertia to fluid forces, which includes fluid inertia and drag;  $\eta$  represents a ratio of blade rigidity to fluid forces (Michelin et al. 2008). The blade's boundary conditions are  $\hat{\zeta}(0, \tau) = 0$ ,  $\theta(0, \tau) = 0$ ,  $\theta_{,s}(1, \tau) = 0$ ,  $\theta_{,ss}(1, \tau) = 0$ , and  $T(1, \tau) = 0$ .

*Parameter ranges for Macrocystis*—Hurd and Pilditch (2011) provided morphological observations (Table 1) that can be used to calculate the dimensionless parameters  $\eta$  and  $\mu$  for *Macrocystis* blades. At flow-sheltered sites, the characteristic velocity is less than 6 cm s<sup>-1</sup> (Kregting et al. 2008; Hurd and Pilditch 2011). At flow-exposed sites, Hurd and Pilditch do not provide a velocity value. We note that at flow-exposed sites, the combination of wave orbital velocities and currents makes it difficult to determine whether the mean, the root mean square (rms), or the maximum velocity is relevant to the kelp. For the purposes of this study, we select a flow-exposed velocity value of 0.50 m s<sup>-1</sup>, but with an uncertainty of +0.45 m s<sup>-1</sup> to account for possible high-velocity events (Duggins et al. 2003). For the flow-sheltered site, we use a velocity of 0.05 m s<sup>-1</sup> with negligible uncertainty, consistent with the

Table 2. Calculations of the dimensionless blade flexural rigidity ( $\eta$ ) based on the observations of Hurd and Pilditch (2011) summarized in Table 1. The exposed morphology value of  $\eta$  is calculated using Eq. 2.

	Exposed morphology	Sheltered morphology
Exposed $U_\infty=0.50 \text{ m s}^{-1}$	$7.1 \times 10^{-5}$	$8.8 \times 10^{-7}$
$U_\infty=0.95 \text{ m s}^{-1}$	$2.0 \times 10^{-5}$	$2.5 \times 10^{-7}$
Sheltered $U_\infty=0.05 \text{ m s}^{-1}$	—	$8.8 \times 10^{-5}$

observations from Hurd and Pilditch (2011). The fluid density is set at  $\rho_f = 1030 \text{ kg m}^{-3}$  and the typical blade density is  $\rho = 1040 \text{ kg m}^{-3}$  (Hale 2001).

In Table 2, we calculate the values of  $\eta$  (the nondimensional rigidity term) for the exposed morphology at the exposed flow velocity and for the sheltered morphology at the sheltered flow velocity. For the sheltered morphology, the flexural rigidity,  $EI = Ebh^3/12$ , and for the exposed morphology, we calculate  $EI$  using Eq. 2, which includes the contribution of corrugations on the blade flexural rigidity. For comparison, we also calculate the value of  $\eta$  for the sheltered morphology at the exposed flow velocity. This calculation allows us to understand how a blade with the sheltered morphology would respond to the flow-exposed velocities. We also calculate the values of  $\eta$  at the flow-exposed velocity of  $0.95 \text{ m s}^{-1}$  to account for the possibility of high-velocity events at these sites. The values of the parameter  $\mu$  for live kelp blades are always small compared with unity (e.g.,  $\mu \leq 1 \times 10^{-3}$ ), indicating that the inertia of the blade has a negligible effect on blade motion. This parameter is not considered further.

*Models for mass flux*—The fluid motion at the surface of kelp blades affects the rate at which the blades acquire nutrients from the surrounding water. Within the turbulent boundary layer at a fluid–solid interface there is a thin layer of fluid with thickness ( $\delta_v$ ), called the viscous sublayer, over which the diffusion of fluid momentum is controlled by the kinematic viscosity of the fluid. Within this sublayer, there is a diffusive sublayer ( $\delta_b$ ). Transport across the diffusive sublayer is controlled by molecular diffusion, which is a much slower process than turbulent diffusion in the bulk of the flow, and therefore this thin layer is the limiting step in mass transfer to the solid interface. In a steady, uniform flow, the thicknesses of the viscous sublayer (Schlichting 1962) and the diffusive sublayer (Boudreau and Jorgensen 2001) can be modeled using the shear velocity at the surface ( $u_*$ ).

$$\delta_v = \frac{5\nu}{u_*} \quad (9)$$

$$\delta_b = \delta_v Sc^{-1/3} \quad (10)$$

The shear velocity is formally defined using the shear stress ( $\tau_w$ ) at the solid interface:  $u_* = (\tau_w/\rho_f)^{1/2}$ , but can also be described empirically using the mean flow velocity as  $u_* = [1/20 \text{ to } 1/5]U_\infty$  (Schlichting 1962). The Schmidt number,  $Sc$

$= \nu/D_W$ , is the ratio of kinematic viscosity ( $\nu$ ) to molecular diffusivity of the species in water ( $D_W$ ). From Eqs. 9 and 10, as the fluid velocity ( $U_\infty$ ) increases, the diffusive sublayer becomes thinner, increasing the rate of mass transfer to the blade surface. The primary assumption of this model is that this diffusive sublayer is steady in thickness. The transfer velocity ( $K$ ) for mass transfer across a steady diffusive sublayer (D.S.L.) can be written as

$$K_{D.S.L.} = \frac{D_W}{\delta_b} \quad (11)$$

In systems with strong turbulent motions, eddies in the flow can transport dissolved species directly to the blade surface, stripping away the diffusive sublayer in a process known as surface renewal (S.R.). When the diffusive sublayer is completely renewed in a periodic manner, the transfer velocity at the interface can be written

$$K_{S.R.} = 2\sqrt{\frac{D_W}{\pi T_R}} \quad (12)$$

where  $T_R$  is the time between surface renewal events (Higbie 1935; Danckwerts 1951). In between these surface renewal events, the diffusive boundary layer regrows over a timescale set by the diffusion coefficient,  $T_D = \delta_b^2/D_W$ . If  $T_R < 0.5T_D$ , then mass transfer can be approximated by Eq. 12. When the renewal period is long, i.e.,  $T_R > 6T_D$ , then the turbulent motions that renew the boundary layer have negligible effect on mass transfer and flux can be modeled using the steady diffusive sublayer model (Eq. 11). For intermediate ratios of  $T_R/T_D$ , the transfer velocity can be modeled as in Stevens et al. (2003).

Ledwell (1984) suggested a variation on the surface renewal model, in which the transport of mass from the bulk of the fluid towards a solid surface is described directly from the normal velocity at the surface. In Ledwell's model, the normal velocity ( $w'$ ) is approximated from conservation of fluid mass at the surface ( $z = 0$ ). It takes the Taylor expansion of the normal velocity ( $w'$ )

$$w'(z) = -(\nabla \times v')_{z=0}z - (\partial \nabla \times v'/\partial z)_{z=0}z^2 + \dots \quad (13)$$

in which  $\nabla \times v'$  is the two-dimensional velocity divergence in a plane parallel to the surface. Higher-order terms in the expansion have been neglected. At a solid interface, the first term is zero, and the normal velocity approaching the interface scales with  $z^2$ . The eddy diffusivity in the fluid,  $D_t$ , can be modeled as a product of the velocity scale (given by Eq. 13) and a mixing length, taken to be the distance from the interface,  $z$ , giving  $D_t \sim (\partial \nabla \times v'/\partial z)_{z=0}z^3$ . The turbulent diffusivity defines a distance from the surface at which eddy motion, represented by  $D_t$ , controls the flux toward the surface, from which Ledwell (1984) derived the following transfer velocity for a solid–liquid interface:

$$K = \frac{3\sqrt{3}}{2\pi} \left( \frac{\partial}{\partial z} (\nabla \times v') \right)_{z=0}^{1/3} D_W^{2/3} \quad (14)$$

A version of the Ledwell model for fluid–fluid interfaces has been successfully used to describe interfacial gas

Table 3. The experimental blade parameters for the six different blades. The upstream velocity ( $U_\infty = 0.2 \text{ m s}^{-1}$ ), blade width ( $b = 0.03 \text{ m}$ ), and blade length ( $l = 0.30 \text{ m}$ ) were held constant for all of the blades.

Material	$h$ ( $\mu\text{m}$ )	$EI/b$ ( $\text{Pa m}^3$ )	$\mu$	$\eta$
LDPE	50	$4.8 \times 10^{-6} \pm 1.8 \times 10^{-6}$	$1.7 \times 10^{-4}$	$4.4 \times 10^{-6}$
LDPE	100	$2.5 \times 10^{-5} \pm 0.6 \times 10^{-5}$	$3.3 \times 10^{-4}$	$2.3 \times 10^{-5}$
LDPE	150	$4.1 \times 10^{-5} \pm 1.1 \times 10^{-5}$	$5.0 \times 10^{-4}$	$3.8 \times 10^{-5}$
LDPE	250	$5.6 \times 10^{-4} \pm 1.0 \times 10^{-4}$	$8.5 \times 10^{-4}$	$5.2 \times 10^{-4}$
UHMWPE	500	$8.3 \times 10^{-3} \pm 1.5 \times 10^{-3}$	$3.4 \times 10^{-3}$	$7.7 \times 10^{-3}$
Aluminum 6061	1000	$6.0 \times 10^0 \pm 1.2 \times 10^0$	$9.1 \times 10^{-3}$	$5.6 \times 10^0$

transfer at the ocean surface; however, no studies have yet verified this model for mass flux at solid–liquid boundaries.

*Laboratory experiments*—We constructed six model blades out of thin, rectangular sections of low-density polyethylene (LDPE), ultrahigh-molecular-weight polyethylene (UHMWPE), and aluminum (width,  $b = 3.0 \text{ cm}$ ; length,  $l = 30.0 \text{ cm}$ ), of different thicknesses, in order to vary the blade flexural rigidity and thus vary  $\eta$ . We selected thicknesses of  $h = 50, 100, 150,$  and  $250 \mu\text{m}$  (LDPE) and  $h = 500 \mu\text{m}$  (UHMWPE). The sixth blade, with thickness  $h = 1000 \mu\text{m}$ , was cut from Aluminum 6061. For each thickness, we measured the blade flexural rigidity ( $EI$ ) with a cantilevered bending test. Short lengths of blades (between 3 and 8 cm) were clamped horizontally in air. The blade sections deflected under their own weight, and the deflection at the free end ( $\delta_{\text{max}}$ ) was used in the linearized Euler-Bernoulli beam equation to estimate flexural rigidity:

$$EI = \frac{q_b l_{\text{sec}}^4}{8\delta_{\text{max}}} \quad (15)$$

where  $q_b = \rho b h g$  is the weight per unit length of the blade section ( $g$  is the gravitational acceleration constant), and  $l_{\text{sec}}$  is the length of the blade section. The six model blades have values of flexural rigidity that span approximately six orders of magnitude, including the range of values relevant to kelp (Table 3). The values of  $\mu$  range from  $1.7 \times 10^{-4}$  to  $9 \times 10^{-3}$ . When  $\mu \ll 1$ , solid inertia can safely be neglected when compared with fluid inertia, which is consistent with the observed values of  $\mu$  for kelp blades found in the environment.

We placed the model blades in a water channel of 38 cm width and 22 cm depth. A regular Kármán vortex street was created at mid-depth using a 1 cm thick bar of height  $D = 2.5$  or  $5.0 \text{ cm}$  that spanned the width of the channel. The vortex street provides a single scale of periodic turbulence

Table 4. The experimental flow parameters for both vortex streets. The vortex street wavelength and Strouhal number (St) change because of the change in flow blockage, which increases from 12.5% to 25% from  $D = 2.5 \text{ cm}$  to  $D = 5.0 \text{ cm}$ .

$U_\infty$ ( $\text{m s}^{-1}$ )	$D$ (cm)	$\lambda$ (cm)	$f$ (Hz)	St
0.2	2.5	15	1.2	0.15
0.2	5.0	20	0.8	0.20

that enables simpler interpretation of blade motion. Whereas the turbulence in open channel flow is broadly distributed over a range of scales and frequencies, the structures in the Kármán vortex street are closely centered around a specific scale and frequency. We measured the vortex street wavelength using particle image velocimetry (Rominger 2014). For  $D = 2.5 \text{ cm}$ , we measured a wavelength of  $6D$ , and for  $D = 5.0 \text{ cm}$ , we measured a wavelength of  $4D$  (Table 4).

In the water channel, the model blades were attached to a slender clamp, which held the blades horizontally at the centerline of the vortex street and a distance  $\Delta x = 4D$  downstream of the bar (Fig. 3). Below the channel false bottom, the clamp was attached to a load cell (Futek LSB210), which recorded the streamwise forces on the clamp plus the model blade at 2 kHz for 300 s. The clamp force was measured separately and subtracted from the total force to give the force on the blade alone. The load cell strain measurements were calibrated with a series of known weights over the range 0–0.006 N, and responded linearly over this range with an error of approximately 9%.

We recorded the instantaneous blade postures with a charge-coupled device camera (DALSA Falcon 1.4M100) at 40 frames per second for 30 s. For these recordings, the blades were illuminated with two 60 W incandescent light fixtures mounted below the glass flume bottom. A black canvas shroud was hung on the back side of the flume to provide a contrasting background to the polyethylene blades. The velocity was characterized from vertical, lateral, and streamwise transects measured using a Nortek Vectrino acoustic Doppler velocimeter. The upstream velocity was  $U_\infty = 0.20 \text{ m s}^{-1}$  for all cases, and was both steady and spatially uniform away from the channel perimeter (i.e.,  $u(x, y, z, t) = U_\infty$ ).

To measure flux to our model blades, we selected two blade thicknesses,  $h = 50 \mu\text{m}$  and  $h = 250 \mu\text{m}$ , which spanned the range of  $\eta$  for *Macrocystis* ( $\eta = 4.4 \times 10^{-6}$  and  $\eta = 5.2 \times 10^{-4}$ , respectively) and which exhibited clear differences in blade motion. We filled the flume 3 d prior to the experiments to allow the water temperature to reach the room temperature of  $23.5^\circ\text{C}$ . We then injected  $70 \mu\text{L}$  of dibromochloromethane ( $\text{CHBr}_2\text{Cl}$ ) in the flowing water and allowed it to fully mix over the entire flume volume ( $2.2 \text{ m}^3$ ). When fully mixed, the concentration of  $\text{CHBr}_2\text{Cl}$  in the flume was near  $80 \mu\text{g L}^{-1}$ .

After the flume was fully mixed, we inserted a model blade into the vortex street for a duration of time,  $T_{\text{exposure}}$ ,

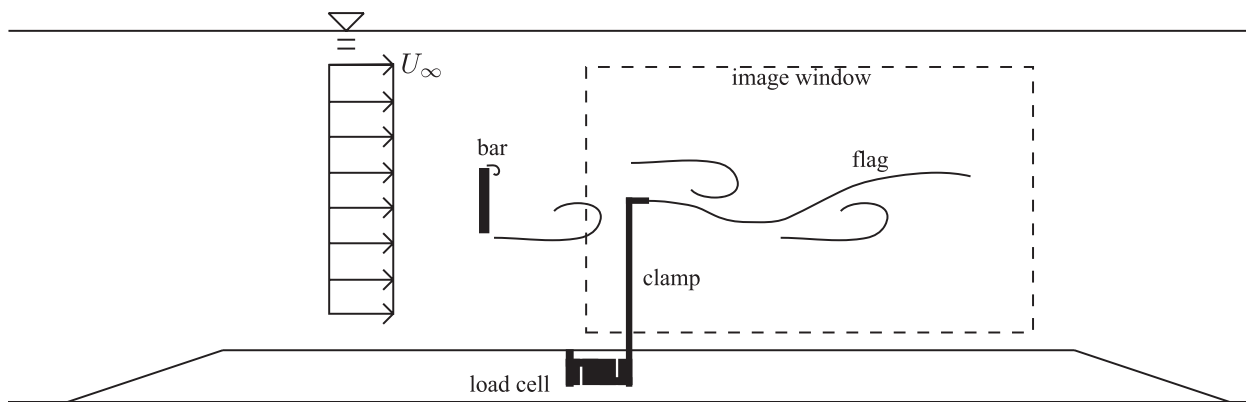


Fig. 3. The experimental setup for the drag and flux experiments. The blade is located at mid-depth and mid-width in the flume, in the centerline of the vortex street. The blade is mounted to a slender clamp, which is fastened to the load cell beneath the flume false bottom.

long enough that  $\text{CHBr}_2\text{Cl}$  diffused into the model blade to a measurable concentration, but short enough that the concentration inside the LDPE blade did not reach equilibrium with the surrounding water. After this exposure time, we removed the blade from the flow and dried the blade with a Kimwipe to remove residual flume water from the blade surface, then inserted the blade into a clean 40 mL amber vial (Qorpak) that was filled with clean water ( $18 \text{ M}\Omega$  at  $25^\circ\text{C}$ ) and then sealed. In the sealed vial, the  $\text{CHBr}_2\text{Cl}$  repartitioned between the LDPE and water phases, ultimately reaching equilibrium. The vials were left for at least 7 d on a shaker table to allow for equilibrium to be reached. This procedure was repeated for increasing time intervals of exposure in the flume with a new LDPE strip used for each new exposure time (Table 5). During each blade exposure trial, the concentration in the flume water was also measured.

After the flume samples were removed from the shaker table, we calculated the mass of  $\text{CHBr}_2\text{Cl}$  in the LDPE indirectly, by measuring the  $\text{CHBr}_2\text{Cl}$  concentration in the water ( $C_{W,\text{vial}}$ ). Because the total mass of  $\text{CHBr}_2\text{Cl}$  remains constant in the sample vial, the initial mass in the LDPE (i.e., the mass accumulated during the experiment) is the sum of the final mass in the LDPE and the final mass in the water:

$$M_{PE} = K_{PEW} C_{W,\text{vial}} V_{PE} + C_{W,\text{vial}} V_W \quad (16)$$

Table 5. The experimental exposure time intervals for the LDPE strips in a vortex street, in the flume containing  $80 \mu\text{g L}^{-1}$   $\text{CHBr}_2\text{Cl}$ .

$T_{\text{exposure}}$ 50 $\mu\text{m}$ LDPE times (s)	$T_{\text{exposure}}$ 250 $\mu\text{m}$ LDPE times (s)
15	60
30	120
60	180
120	300
180	600
300	900
600	1200

where we have used the polyethylene water partition coefficient ( $K_{PEW}$ ) to find the concentration in the polyethylene,  $C_{PE,\text{vial}} = K_{PEW} C_{W,\text{vial}}$ .

The partition coefficient between water and the LDPE strips ( $K_{PEW}$ ) for  $\text{CHBr}_2\text{Cl}$  was measured with an equilibration experiment. We placed clean model blades in 40 mL amber vials that contained a known initial concentration of  $\text{CHBr}_2\text{Cl}$  in the water phase ( $C_{W,i}$ ). Upon reaching equilibrium, we remeasured the concentration of  $\text{CHBr}_2\text{Cl}$  in the water phase ( $C_{W,\text{measure}}$ ). Because the total mass of  $\text{CHBr}_2\text{Cl}$  remains constant throughout the partitioning experiment, the partition coefficient could be determined from mass balance:

$$K_{PEW} = \frac{C_{W,i} V_W - C_{W,\text{measure}} V_W}{C_{W,\text{measure}} V_{PE}} \quad (17)$$

in which  $V_W$  is the volume of water in the vial and  $V_{PE}$  is the volume of the polyethylene blade. The values estimated from this method were  $K_{PEW} = 300 \pm 30$  for  $h = 50 \mu\text{m}$  and  $K_{PEW} = 100 \pm 15$  for  $h = 250 \mu\text{m}$ .

During each blade flux measurement, the  $\text{CHBr}_2\text{Cl}$  concentration in the flume water sample was analyzed as well. The concentration in the flume water ( $C_{W,\text{flume}}$ ) was used to calculate the theoretical equilibrium mass in the polyethylene,  $M_{PE,\infty} = C_{W,\text{flume}} K_{PEW} V_{PE}$ . The decrease in concentration in the flume water was negligible over the course of the series of experiments. Specifically, the concentration in the flume decreased by 2% over a period of 4 h, whereas the longest experimental time point was 20 min (Table 5).

We measured the concentration of  $\text{CHBr}_2\text{Cl}$  in the vial water (for both the vials containing LDPE strips and vials containing flume water samples) using a purge and trap (Tekmar LSC 2000) in concert with a gas chromatograph and electron capture detector (GC-ECD; Perkin Elmer Autosystem XL). Vial water samples of 5 mL volume were injected into the purge and trap for purge times of between 0.25 and 1.00 min (depending on the anticipated water concentration). The purge and trap was held at a standby temperature of  $30^\circ\text{C}$  and the desorb was set at  $225^\circ\text{C}$  for 2.00 min. After each sample, the trap was baked for

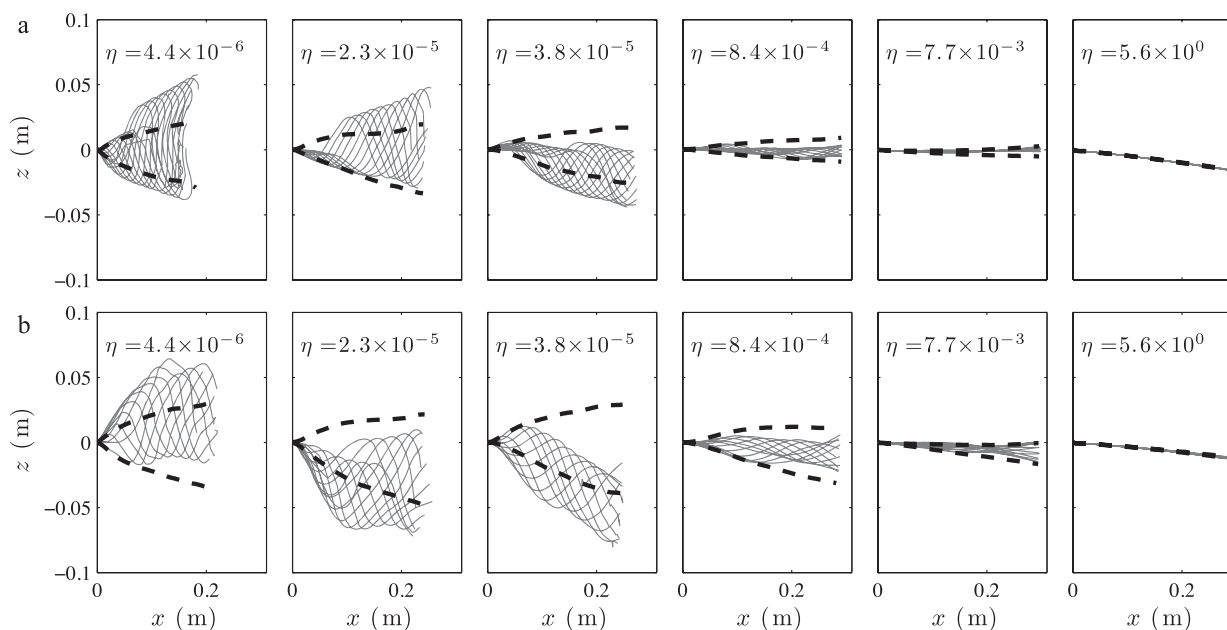


Fig. 4. Selected instantaneous postures observed in the (a)  $D = 2.5$  cm and (b)  $D = 5.0$  cm vortex streets overlaid for one vortex period. Relative blade rigidity ( $\eta$ ) increases from left to right. When present, the postures were selected to demonstrate the asymmetric oscillations. The rms envelope of blade postures about the blade's mean posture, based on the full 30 s record, is shown by the bold dashed lines. The blade at  $\eta = 5.6 \times 10^0$  exhibits a slight downward bias in its mean posture because of its weight (material is Aluminum 6061). Note that the vertical axis is exaggerated.

10.00 min at  $230^\circ\text{C}$ . After desorption, the purge and trap injects the purged portion of the sample directly into the gas chromatograph column (Agilent DB-624 column with a  $1.80 \mu\text{m}$  film and  $0.320$  mm bore,  $60$  m in length). The initial column temperature was set at  $40^\circ\text{C}$ , and was held at  $40^\circ\text{C}$  for  $0.50$  min before being increased at a rate of  $10^\circ\text{C min}^{-1}$  until it reached a temperature of  $200^\circ\text{C}$ . The GC-ECD output was calibrated with a series of  $\text{CHBr}_2\text{Cl}$  standards of concentrations between  $0.04$  and  $80 \mu\text{g L}^{-1}$  and at purge times of between  $0.25$  and  $4.00$  min. We measured multiple water samples ( $\geq 3$ ) from each experimental vial in order to calculate the instrument uncertainty.

With the time series of normalized mass acquired over specified exposure times, we constructed an equilibration curve, from which we extracted a transfer velocity. However, as mass transfer to the polyethylene is a function of both the transfer velocity through the fluid and diffusion inside the polyethylene, extracting the transfer velocity required modeling the diffusion within the LDPE blade. We solved the one-dimensional ( $z$ ) diffusion equation over the blade thickness (Eq. 18). We neglected lateral and longitudinal diffusion within the PE based on the fact that the lateral and longitudinal diffusion timescales are long compared with the vertical ( $z$ ) diffusion timescale, i.e.,  $h^2/D_{PE} \ll l^2/D_{PE}$  and  $b^2/D_{PE}$ , with  $D_{PE}$  the molecular diffusion coefficient within the LDPE. We assumed the following boundary conditions: no net flux at the strip centerline because of symmetry (Eq. 19) and a prescribed transfer velocity,  $K$ , at the strip surface (Eq. 20).

$$\frac{\partial C_{PE}}{\partial t} = D_{PE} \frac{\partial^2 C_{PE}}{\partial z^2} \quad (18)$$

$$\left. \frac{\partial C_{PE}}{\partial z} \right|_{z=0} = 0 \quad (19)$$

$$D_{PE} \left. \frac{\partial C_{PE}}{\partial z} \right|_{z=h/2} = \Delta CK \quad (20)$$

where  $C_{PE}$  is the concentration of  $\text{CHBr}_2\text{Cl}$  within the LDPE and  $\Delta C$  is the concentration difference between the surface of the blade and the bulk of the fluid.

We solved Eqs. 18–20 using an implicit finite difference (FD) method. To calculate the experimental transfer velocity for each model blade ( $h = 50 \mu\text{m}$  and  $h = 250 \mu\text{m}$ ), we used the FD model to find the transfer velocity that minimizes the sum-of-squares error between the model and the experimental data set. This process was repeated for the bounds of the 95% confidence interval (C.I.) on the diffusion coefficient within the LDPE, producing a different experimental transfer velocity for each modeled diffusion coefficient.

## Results

*Blade motion and drag force*—The instantaneous blade postures extracted from the digital images (Fig. 4) show that as  $\eta$  decreases, the oscillation amplitude increases. This trend is evident in both the instantaneous postures and the

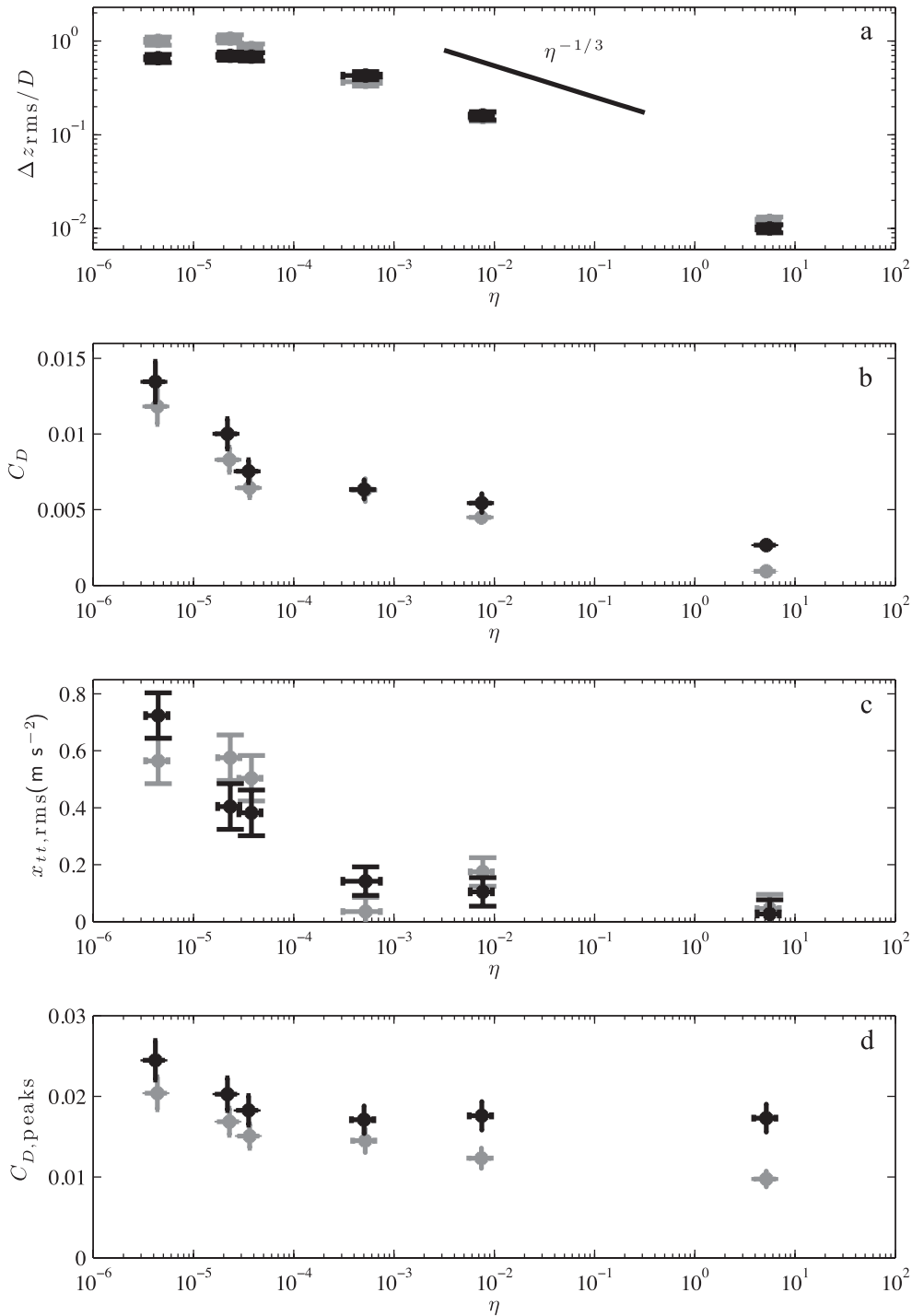


Fig. 5. (a) The measured rms amplitude of blade motion at  $s = 1$  normalized by  $D$ , plotted against the relative blade rigidity ( $\eta$ ). The scaling predicted from the balance of fluid torque and the elastic bending moment is shown with the solid line. Below  $\eta = 1 \times 10^{-4}$ ,  $\Delta z_{\text{rms}}$  saturates near the vortex street height. (b) Measured, time-averaged drag coefficient vs. relative blade rigidity ( $\eta$ ). The slope of  $C_D$  vs.  $\eta$  shows a clear transition near  $\eta = 1 \times 10^{-4}$ . (c) The rms streamwise acceleration measured at  $s = 1$ . (d) The average, instantaneous peak drag coefficient on the blade over a vortex street cycle as a function of  $\eta$ . The data for  $D = 2.5$  cm ( $l/D = 12$ ) is plotted with the gray symbols and lines, and the data for  $D = 5.0$  cm ( $l/D = 6$ ) is plotted with the black symbols and lines.

rms envelope of the entire 30 s record, indicated by the dashed lines in Fig. 4. For the most flexible blades, i.e.,  $\eta < 1 \times 10^{-4}$ , we observed instances in which the blades oscillated asymmetrically, either in the upper half or the

lower half of the vortex street, whereas for the more rigid blades, the oscillations were primarily symmetric about the vortex street centerline. The asymmetric oscillations were generally observed over only 1 or 2 vortex periods before

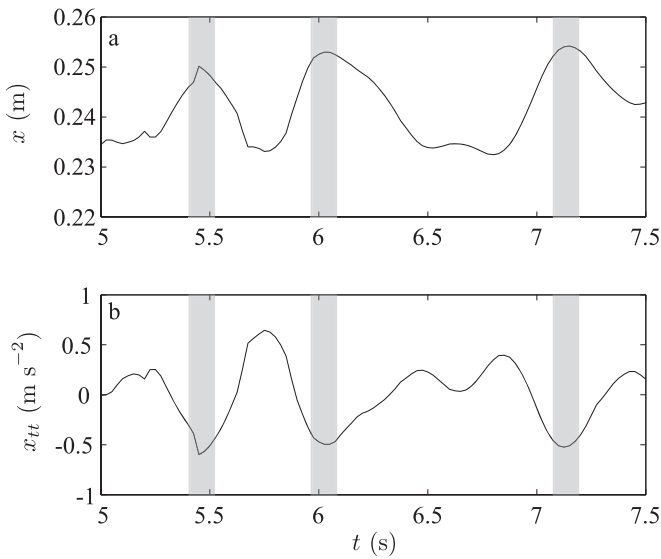


Fig. 6. (a) A sample time record of the streamwise ( $x$ ) blade tip position and (b) streamwise blade tip acceleration for  $\eta = 2.3 \times 10^{-5}$  and  $D = 2.5$  cm. Three examples of downstream motions that are rapidly arrested, producing large negative accelerations, and that translate into tensile forces are highlighted with the gray bars.

the blade reverted to oscillations that were approximately symmetric about the vortex street centerline. Using the full 30 s record, we characterized the oscillation amplitude using the rms value of the vertical distance from the blade tip to the vortex street centerline,  $\Delta z_{\text{rms}}$  (Fig. 5a), which was largest for the smallest values of  $\eta$  and decreased as  $h$  was increased. Below  $\eta \approx 1 \times 10^{-4}$ , the oscillation amplitude no longer changes with  $\eta$  but remains constant because it is limited near the height of the vortex street, which is the limit of the fluid forcing. When normalized by the vortex street height, the blade's amplitude response is the same for both vortex street heights.

Because solid inertia is negligible ( $\mu \ll 1$ ), we can derive a scaling relationship between  $\Delta z_{\text{rms}}$  and  $\eta$  by balancing the fluid torque and the elastic bending moment ( $EI\theta_s$ ). The vertical velocity component of the vortex street is directly proportional to  $U_\infty$  (Alben 2009), and it is this vertical velocity that deflects the blade vertically. The scale of the vertical force on the blade is then  $\rho_f U_\infty^2 b l$ , which exerts a torque that scales with  $\rho_f b l^2 U_\infty^2$ . If curvature is confined to a fraction of the blade length, we scale  $\theta_s$  using a bending length scale,  $l_o < l$ , giving  $\theta \sim \Delta z_{\text{rms}}/l_o$  and  $\theta_s \sim \Delta z_{\text{rms}}/l_o^2$ . We consider whether the bending length scale defined for steady deflection in Alben et al. (2002),  $l_o = (EI/\rho_f b U_\infty^2)^{1/3}$ , can be applied to this unsteady system. This formulation yields  $\Delta z_{\text{rms}} \sim l\eta^{-1/3}$ , or  $\Delta z_{\text{rms}}/D \sim (l/D)\eta^{-1/3}$ , which is plotted with the experimental data in Fig. 5a. This scaling relationship is consistent with the observed trends in  $\Delta z_{\text{rms}}$  vs.  $\eta$  for  $\eta \gtrsim 1 \times 10^{-4}$  (Fig. 5a), which suggests that unsteady responses in the low solid inertia regime are governed by the same bending length scale as steady responses.

The normalized drag force has no dependence on vortex street size, as the measurements in the two vortex streets ( $D$

= 2.5 and 5 cm) are in agreement within uncertainty (Fig. 5b). This is due to the similarity of the mean velocity profiles in the vortex street wakes when scaled by  $D$ . As the blade oscillation amplitude in both vortex streets is the same when normalized by  $D$  (Fig. 5a), the blades encounter the same mean velocity profile, despite having different absolute oscillation amplitudes.

We next consider the normalized drag, represented by the blade drag coefficient ( $C_D$ ), defined as

$$C_D = \frac{F_D}{\rho_f b l U_\infty^2} \quad (21)$$

Above  $\eta \approx 1 \times 10^{-4}$ , the measured drag coefficients decrease gradually as  $\eta$  is increased, following a trend similar to the oscillation amplitude (Fig. 5a). This result suggests that above  $\eta \approx 1 \times 10^{-4}$ , drag is primarily determined by blade frontal area, which is proportional to oscillation amplitude. Below  $\eta \approx 1 \times 10^{-4}$ , the drag increases more rapidly as  $\eta$  is decreased. This occurs despite the fact that the oscillation amplitude remains constant below  $\eta \approx 1 \times 10^{-4}$ , indicating that in this range drag is no longer correlated to oscillation amplitude. To explain this behavior, we analyze the blade acceleration.

In addition to the vertical motion, which we have characterized by  $\Delta z_{\text{rms}}$ , the interaction with the passing vortices also causes the blade tip ( $s = 1$ ) to move both upstream and downstream. The downstream portion of the blade motion is constrained by the blade length and the blade's inextensibility. As the blade reaches its full length, streamwise motion at the blade tip is rapidly arrested, creating a high negative acceleration and a high instantaneous tensile force in the blade (Denny et al. 1998). Although there are large accelerations during upstream motion, this motion is not constrained by the blade's inextensibility and therefore does not produce a corresponding response in the blade's internal tension. We characterize these periods of high acceleration with the rms of streamwise acceleration at the blade tip (Fig. 5c). The blades with periods of high tip acceleration are also the blades that show an increase in the time-averaged force on the blade (Fig. 5b). In Fig. 6, we have plotted the streamwise position of the blade tip ( $s = 1$ ) and have highlighted the resulting spikes in acceleration. Aside from occasional aperiodic behavior due to randomness in the flow field, these acceleration peaks occur regularly at the vortex street frequency.

We also consider changes in the instantaneous force, which can cause high mechanical stresses and strains within the kelp blade that can lead to either blade breakage or dislodgment of the entire kelp frond (Denny et al. 1998). In Fig. 5d, we plot the average of the peak drag coefficient within each vortex cycle. The peak drag coefficients are significantly higher than the time-averaged drag; however, they follow the same broad trend as the mean drag coefficients. Notably, the peak drag (Fig. 5d) is directly correlated with the tip acceleration (Fig. 5c).

*Flux results*—Figure 7 presents the best fit between the measured and modeled mass accumulation within the

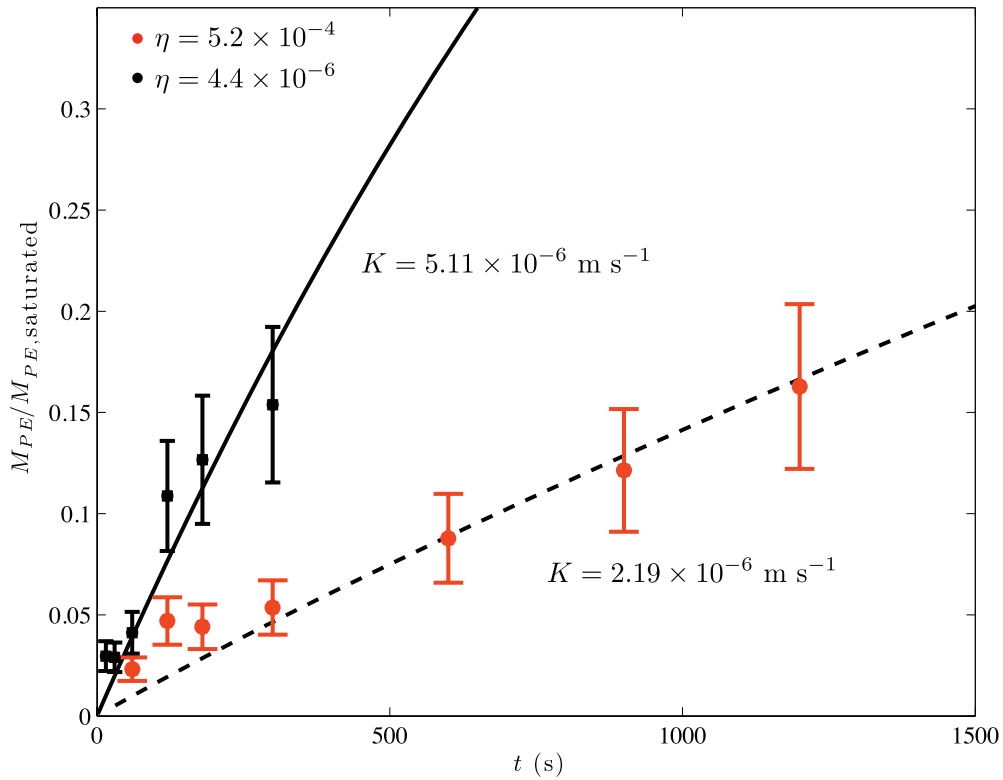


Fig. 7. The data series of mass accumulation within the LDPE blades normalized by the equilibrium mass accumulation,  $M_{PE,\infty}$  vs. time for both blade thicknesses:  $h = 50 \mu\text{m}$  ( $\eta = 4.4 \times 10^{-6}$ ) and  $h = 250 \mu\text{m}$  ( $\eta = 5.2 \times 10^{-4}$ ). The modeled mass accumulation curves use the best-fit transfer velocities. The curves are plotted with a solid line:  $h = 50 \mu\text{m}$  ( $\eta = 4.4 \times 10^{-6}$ ), and dashed line:  $h = 250 \mu\text{m}$  ( $\eta = 5.2 \times 10^{-4}$ ).

blade, showing that the best-fit transfer velocity was higher for  $h = 50 \mu\text{m}$  ( $\eta = 4.4 \times 10^{-6}$ ) than for  $h = 250 \mu\text{m}$  ( $\eta = 5.2 \times 10^{-4}$ ; Table 6). That is, the more flexible blade, which responds to the vortex street with larger amplitude oscillations (Fig. 5a) has a higher rate of flux. The 95% C.I.s for the two blade thicknesses, which span two orders of magnitude, do not overlap, further confirming that the measured difference is significant. As both blades oscillate in the vortex street at the same frequency (the vortex street frequency), it follows that the blade that with larger amplitude motion has a higher relative velocity. Indeed, numerical modeling of blade motion in a vortex street confirmed that more flexible blades have higher relative fluid velocity at their surface (Rominger 2014).

### Discussion

Our measurements have demonstrated that the drag force on a model kelp blade is a strong function of the blade flexural rigidity. Specifically, as the nondimensional blade flexural rigidity decreases, the blade responds to vortex passage with oscillations of increasing amplitude (Fig. 5a). Below a critical value of the nondimensional blade flexural rigidity, blade acceleration forces become important, and the resulting total force increases sharply with decreasing  $\eta$  (Fig. 5b). The experiments suggest that the critical value of  $\eta$  below which blade acceleration forces become important is  $\eta = 1 \times 10^{-4}$  (Fig. 5b). In Table 2, we estimate that a sheltered morphology transplanted to an

Table 6. The calculated experimental transfer velocities that minimize the sum of squares error between the modeled and measured time series of mass accumulation. The transfer velocities were also calculated for the bounds of the 95% C.I. on the LDPE diffusion coefficient. The last row of the table includes the predictions for the transfer velocities and the transfer velocity ratio from the simplified model of Eqs. 22 and 24 for  $D = 2.5 \text{ cm}$ .

$D_{PE} \text{ (m}^2 \text{ s}^{-1}\text{)}$	$K \text{ (m s}^{-1}\text{) for } h = 50 \mu\text{m}$	$K \text{ (m s}^{-1}\text{) for } h = 250 \mu\text{m}$	$K_{h=50 \mu\text{m}}/K_{h=250 \mu\text{m}}$
$10^{-10.3}$	$5.0 \times 10^{-6}$	$1.9 \times 10^{-6}$	2.6
$10^{-11.3}$	$5.1 \times 10^{-6}$	$2.2 \times 10^{-6}$	2.3
$10^{-12.3}$	$6.2 \times 10^{-6}$	$4.6 \times 10^{-6}$	1.4
Model-predicted	$4.9 \times 10^{-6}$	$3.8 \times 10^{-6}$	1.3

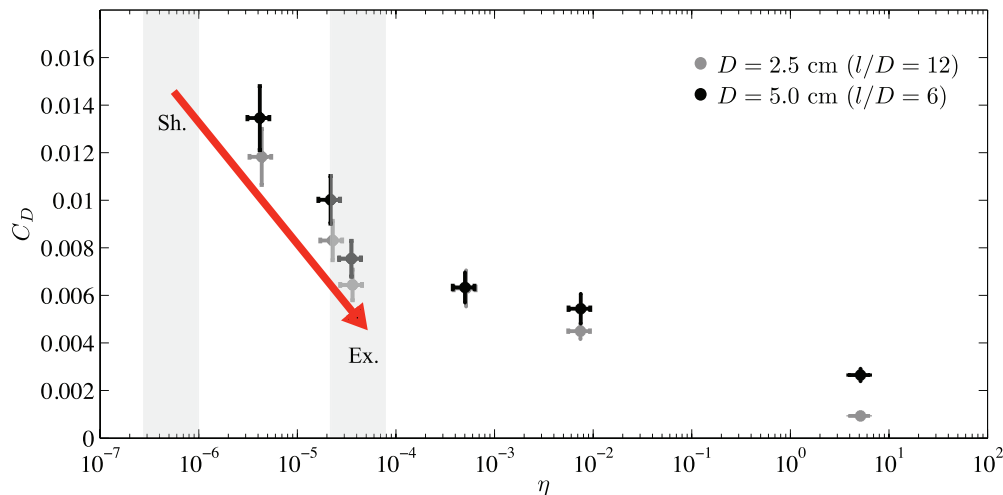


Fig. 8. The measured drag coefficients (from Fig. 5b), plotted on an expanded axis to show the potential reduction in drag caused by the shift from the sheltered morphology to the exposed morphology. The red arrow points from the value of  $\eta$  of the sheltered morphology (Sh.) to the value of  $\eta$  for the exposed morphology (Ex.), both calculated at the exposed flow velocity. The  $\eta$  values from Table 2 are indicated with the vertical gray bars. The increase in blade flexural rigidity at the flow-exposed site prevents an increase in drag due to enhanced flapping and inertial forces in response to turbulence.

exposed site would fall in the range of  $\eta = 2.5 \times 10^{-7}$  to  $8.8 \times 10^{-7}$ , which is far below this critical value, suggesting that the transplanted blade would experience high and potentially damaging peak forces. In contrast, the exposed morphology at an exposed site falls in the range of  $\eta = 2.0 \times 10^{-5}$  to  $7.1 \times 10^{-5}$ , two orders of magnitude larger than the sheltered morphology at the exposed flow velocity. This adjustment, depicted in Fig. 8, should reduce both the total and instantaneous forces on the blade. Interestingly, the values of  $\eta$  for both the exposed and sheltered morphologies, at their respective flow velocities, are very close in magnitude, suggesting that there may be an optimal ratio of blade stiffness to fluid forcing, towards which the kelp morphology adjusts. Although lower values of  $\eta$  result in higher drag forces on the blade, higher values of  $\eta$  could indicate unnecessary and biologically expensive structural strengthening. Below, we also consider what advantages in nutrient acquisition might be associated with lower values of  $\eta$ .

In a vortex street, the turbulence is narrowly centered around a single frequency and wavelength. However, our experiments indicate that the blade responds to each passing vortex. Therefore, it is likely that similar behavior could be observed for blades subjected to the spectrum of turbulent and wave orbital fluctuations in the coastal ocean, i.e., blades with low flexural rigidity would be subjected to high inertial forces. Indeed, flexible models of entire kelp fronds subject to a range of wave frequencies were observed to experience high inertial forces, often associated with chaotic motion (Denny et al. 1997). Further, Denny et al. (1998) examine the response of organisms across a range of fluid motion and demonstrate how inertial forces have maximums associated with particular frequencies.

Our experimental measurements of mass flux suggest higher fluxes are achieved for the more flexible blade, which experienced greater blade movement and higher relative velocity. This is consistent with the results of Denny and Roberson (2002) and Koehl and Alberte (1988), who studied flux at the surface of rigid model blades and of live kelp blades, respectively. Denny and Roberson oscillated rigid model blades at increasing frequencies and found that over a certain range of flow speeds, increasing the frequency (i.e., increasing the relative blade velocity) increased flux. Koehl and Alberte found that blades that flapped more had higher rates of photosynthesis, due to higher rates of carbon uptake at the blade surface.

Together, the mass flux and drag experiments in this study show that changes in blade flexural rigidity not only modulate fluid drag forces, but may also affect the rate of mass flux at the blade surface. Previous observations of live kelp blades show that blades increase their flexural rigidity in more flow-exposed environments. At the same time, there is an increase in the characteristic fluid velocity in flow-exposed environments. The combined result of the changes in blade flexural rigidity together with the changes fluid velocity is that the ratio  $\eta$  remains approximately constant. By maintaining a higher value of  $\eta$ , the kelp reduces the drag forces it experiences, but also reduces the transfer velocity that controls nutrient flux to the blade. It may seem counterintuitive that kelp would adapt in a manner that reduces its ability to acquire nutrients. However, based on previous experimental studies, it has been found that in flow-exposed environments, kelp can already acquire nutrients at a rate that exceeds its nutrient requirements. Indeed, various studies on uptake rates of different essential nutrients have found that uptake rates saturate at mean flow velocities between 2 and 6  $\text{cm s}^{-1}$

(Gerard 1982a; Koehl and Alberte 1988; Hurd et al. 1996). This means that at high fluid velocities, nutrients are delivered to the blade surface faster than the nutrients can be utilized and/or stored by the kelp. Understanding that nutrient flux is not a limiting process, we conclude that in high-flow environments, the kelp adapts its morphology predominantly to reduce drag.

The formation of corrugations represents a unique adaptation to flow-exposed environments. As opposed to the alternative mechanism for increasing blade flexural rigidity, i.e., increasing blade thickness, the formation of corrugations can maintain the ratio of blade surface area to blade volume, which may be important for nutrient uptake. In addition, with corrugations, the same rigidity can be achieved with less material, i.e., it is a more efficient method to increase flexural rigidity. We expect that the junctions and mergers of corrugations on natural blades have minimal effect on the enhanced rigidity. Unless all corrugations abruptly end at the same location along the blade (which we have not observed), localized weak points will be distributed and the net effect of the corrugations will remain a significant increase in rigidity.

We now examine how well the common models for transfer velocity (Eqs. 11 and 12) describe the values observed in this study. We first consider the steady diffusive sublayer. We assume that the leading edge of the blade trips the boundary layer into a turbulent boundary layer state. For a mean flow speed  $U_\infty = 0.20 \text{ m s}^{-1}$ ,  $u_* = 0.01$  to  $0.04 \text{ m s}^{-1}$ , and the laminar sublayer thickness, using Eq. 9, is  $\Delta_y = 1.25 \times 10^{-4}$  to  $5 \times 10^{-4} \text{ m}$ . The diffusive sublayer thickness (Eq. 10), is between  $1.25 \times 10^{-5}$  and  $5 \times 10^{-5} \text{ m}$ . This thickness produces a transfer velocity of between  $K_{D,B.L.} = 2 \times 10^{-5}$  and  $8 \times 10^{-5} \text{ m s}^{-1}$ . These values are much larger than the measured transfer velocity for the  $h = 50 \text{ }\mu\text{m}$  and  $h = 250 \text{ }\mu\text{m}$  blades of between  $2 \times 10^{-6}$  and  $6 \times 10^{-6} \text{ m s}^{-1}$  (Table 6). Moreover, the steady diffusive boundary layer model cannot differentiate between the two values of flexural rigidity, and thus cannot predict the observed differences in flux.

We next consider the surface renewal model, assuming that the vortex frequency determines the frequency of boundary layer disturbance. For the  $D = 2.5 \text{ cm}$  vortex street,  $f = 1.2 \text{ Hz}$ , or  $T_R = 0.83 \text{ s}$ . For these parameters, the classic surface renewal model (Eq. 12) predicts a transfer velocity of  $K_{S,R} = 3.92 \times 10^{-5} \text{ m s}^{-1}$ . This transfer velocity is an order of magnitude larger than the measured transfer velocity. A possible explanation for the over-prediction is that the diffusive sublayer is not completely stripped with each disturbance, as the model assumes, but is only partially thinned. In addition, the surface renewal model cannot differentiate between the two blades in our experiments, because they oscillate at the same frequency.

Finally, we consider the Ledwell model (Eq. 14), which connects flux to the surface-normal velocity. This mass transfer model was developed for a stationary boundary, but we adapted it here to a moving boundary using the relative instead of the absolute velocity. Instead of reconstructing the surface-normal velocity through the use of continuity, we use observations and scaling to estimate the surface-normal relative velocity scale,  $w_{\text{rel,rms}}$ .

We note that flow approaching a solid obstruction diverges at a distance that scales with the obstruction width. Based on this, we assume that the length scale of divergence for the normal velocity approaching the blade will be the blade width,  $b$ . With these adjustments, Ledwell's model can be written

$$K = \frac{3\sqrt{3}}{2\pi} \left( \frac{w_{\text{rel,rms}}(s)}{b^2} \right)^{1/3} D_w^{2/3} \quad (22)$$

We approximate the blade normal velocity from the blade oscillation amplitude and frequency. By fitting the scale prediction  $\Delta z_{\text{rms}}/l \sim \eta^{-1/3}$  to the observed oscillation amplitude (Fig. 5a), we derived an empirical expression for amplitude at the blade tip.

$$\Delta z_{\text{rms}} = \frac{l\eta^{-1/3}}{258} \quad (23)$$

Combining Eq. 23 with the frequency of oscillation gives an approximate average blade-normal velocity,  $w_{\text{blade}} = (l\eta^{-1/3})/129$ . The relative normal velocity at the blade surface is a combination of  $w_{\text{blade}}$  and the normal component of the fluid velocity ( $w_{\text{flow}}$ ). Within the vortex street,  $w_{\text{flow}} = 0.4U_\infty$ . The two velocity components do not sum linearly, however, because of the potential for a phase difference between the blade and fluid motion. For a conservative estimate, we sum the blade and fluid velocities in quadrature.

$$w_{\text{rel,rms}} = \sqrt{w_{\text{blade}}^2 + w_{\text{flow}}^2} \quad (24)$$

Using  $w_{\text{rel,rms}}$  in Eq. 22, we predict the following transfer velocities:  $K_{h=50 \text{ }\mu\text{m}} = 4.9 \times 10^{-6} \text{ m s}^{-1}$  and  $K_{h=250 \text{ }\mu\text{m}} = 3.8 \times 10^{-6}$ , and a transfer velocity ratio of  $K_{h=50 \text{ }\mu\text{m}}/K_{h=250 \text{ }\mu\text{m}} = 1.3$  (Table 6). The predicted transfer velocities are within 5% of the experimental value for  $K_{h=50 \text{ }\mu\text{m}}$  and within a factor of two for  $K_{h=250 \text{ }\mu\text{m}}$ , which is much better agreement than produced by either the surface renewal or diffusive sublayer models. Importantly, the relative velocity model captures the increase in flux observed experimentally between the two blades. Specifically, with a decrease in nondimensional blade rigidity,  $\eta$ , the predicted transfer velocity increases by a factor of 1.3. Therefore, an adaptation of the Ledwell model and a simplified approximation for  $w_{\text{rel,rms}}$  provide a reasonable prediction for the transfer velocity to a flexible blade.

For a flat plate oriented parallel to the mean flow direction, we expect that the mass flux and momentum flux to the plate should scale similarly. This concept is called the Reynolds analogy for heat and momentum flux (Reynolds 1874; Deen 1998; Welty et al. 2001). The Reynolds analogy is specifically valid in cases where there is no form (pressure) drag, and momentum flux is entirely due to friction. This analogy has been extended to coral reef communities (Thomas and Atkinson 1997), in which the stress exerted on the flow by the reef can be described with a friction coefficient. In our experiments, not only is form drag present because of the large-amplitude oscillations, which present a frontal area normal to the flow, but inertial forces also contribute to the total measured force on the

model blades. The Reynolds analogy has not been extended to cases where there are inertial forces, and there is currently no theoretical support for the similarity between scalar and momentum flux extending to this regime. However, we can explore the possible extension of the Reynolds analogy to flexible boundaries using our measurements. The ratio of the drag force, or momentum flux, for these blades was  $F_{D,h=50\ \mu\text{m}}/F_{D,h=250\ \mu\text{m}} = 1.8 \pm 0.2$ . The ratio of the mass transfer velocities was  $K_{h=50\ \mu\text{m}}/K_{h=250\ \mu\text{m}} = 2.0 \pm 0.6$ , based on the uncertainty in  $D_{PE}$  (see Table 6). The ratios of drag and flux agree within uncertainty. Therefore, our results provoke the possibility that there exists a similarity between scalar and momentum flux for a flexible body moving in flow.

To conclude, this study demonstrates, through a simple experimental configuration, the role that blade flexural rigidity plays in altering the drag force and the rate of mass flux at the blade surface. As the dimensionless flexural rigidity decreases, blade drag force increases. The dependence on  $\eta$  is particularly strong below the threshold of  $\eta = 10^{-4}$ . This shift to higher drag with smaller nondimensional rigidity may explain the observed shift to a stiffer morphology in flow-exposed environments. Similarly, as the dimensionless flexural rigidity decreases, mass flux to the blades increases. Both the diffusive sublayer and traditional surface renewal models failed to predict the observed mass flux. An adaptation to the Ledwell model, which reflects the relative velocity between the blade and the fluid, does reasonably well in predicting the observed mass fluxes. This highlights the importance of relative velocity, as opposed to current or blade motion individually, as the better predictor for trends in flux.

#### Acknowledgments

This material is based upon work supported by the National Science Foundation under grant EAR-1140970. We also thank two anonymous reviewers for their comments, which greatly improved this manuscript.

#### References

- ALBEN, S. 2009. Passive and active bodies in vortex-street wakes. *J. Fluid Mech.* **642**: 99–125.
- , AND M. SHELLEY. 2008. Flapping states of a flag in an inviscid fluid: bistability and the transition to chaos. *Phys. Rev. Lett.* **100**: 074301, doi:10.1103/PhysRevLett.100.074301
- , AND J. ZHANG. 2002. Drag reduction through self-similar bending of a flexible body. *Nature* **420**: 479–481, doi:10.1038/nature01232
- BOUDREAU, B., AND B. JORGENSEN [EDS.]. 2001. The benthic boundary layer. Oxford.
- BRIASSOULIS, D. 1986. Equivalent orthotropic properties of corrugated sheets. *Comput. Struct.* **23**: 129–138, doi:10.1016/0045-7949(86)90207-5
- CHESHIRE, A., AND N. HALLAM. 1989. Morphological differences in the southern bull-kelp (*Durvillaea potatorum*) throughout south-eastern Australia. *Bot. Mar.* **32**: 191–197.
- DANCKWERTS, P. 1951. Significance of liquid-film coefficients in gas absorption. *Ind. Eng. Chem.* **43**: 1460–1467, doi:10.1021/ie50498a055
- DATTA, S., AND W. GOTTENBERG. 1975. Instability of an elastic strip hanging in an airstream. *J. Appl. Mech.* **42**: 195, doi:10.1115/1.3423515
- DEEN, W. 1998. Analysis of transport phenomena. Oxford.
- DENNY, M., B. GAYLORD, AND E. COWEN. 1997. Flow and flexibility II. The roles of size and shape in determining wave forces on the bull kelp *Nereocystis luetkeana*. *Exp. Biol.* **200**: 3165–3183.
- , B. HELMUTH, AND T. DANIEL. 1998. The menace of momentum: Dynamic forces on flexible organisms. *Limnol. Oceanogr.* **43**: 955–968, doi:10.4319/lo.1998.43.5.0955
- , AND L. ROBERSON. 2002. Blade motion and nutrient flux to the kelp *Eisenia arborea*. *Biol. Bull.* **203**: 1–13, doi:10.2307/1543453
- DRUEHL, L., AND L. KEMP. 1982. Morphological and growth responses of geographically isolated *Macrocystis integrifolia* populations when grown in a common environment. *Can. J. Bot.* **80**: 1409–1413, doi:10.1139/b82-179
- DUGGINS, D., J. ECKMAN, C. SIDON, AND T. KLINGER. 2003. Population, morphometric and biomechanical studies of three understory kelps along a hydrodynamic gradient. *Mar. Ecol. Prog. Ser.* **265**: 57–76, doi:10.3354/meps265057
- ELOY, C., R. LAGRANGE, C. SOUILLIEZ, AND L. SCHOUVEILER. 2008. Aeroelastic instability of cantilevered flexible plates in uniform flow. *J. Fluid Mech.* **611**: 97–106, doi:10.1017/S002211200800284X
- GERARD, V. 1982a. In situ rates of nitrate uptake by giant kelp, *Macrocystis pyrifera* (L.) C. Agardh: Tissue differences, environmental effects, and predictions of nitrogen-limited growth. *J. Exp. Mar. Biol. Ecol.* **62**: 211–224, doi:10.1016/0022-0981(82)90202-7
- . 1982b. In situ water motion and nutrient uptake by the giant kelp *Macrocystis pyrifera*. *Mar. Biol.* **69**: 51–54, doi:10.1007/BF00396960
- , AND K. MANN. 1979. Growth and production of *Laminaria longicuris* (Phaeophyta) populations exposed to different intensities of water movement. *J. Phycol.* **15**: 33–41, doi:10.1111/j.0022-3646.1979.00033.x
- HALE, B. 2001. Macroalgal materials: Foiling fracture and fatigue from fluid forces. Ph.D. thesis, Stanford Univ.
- HARING, R., AND R. CARPENTER. 2007. Habitat-induced morphological variation influences photosynthesis and drag on the marine macroalga *Pachidictyon coriaceum*. *Mar. Biol.* **151**: 243–255, doi:10.1007/s00227-006-0474-2
- HEPBURN, C., J. HOLBOROW, S. WING, R. FREW, AND C. HURD. 2007. Exposure to waves enhances the growth rate and nitrogen status of the giant kelp *Macrocystis pyrifera*. *Mar. Ecol. Prog. Ser.* **339**: 99–108, doi:10.3354/meps339099
- HIGBIE, R. 1935. The rate of absorption of a pure gas into a still liquid during short periods of exposure. *Trans. Am. Inst. Chem. Eng.* **31**: 365–389.
- HUANG, I., J. ROMINGER, AND H. NEPF. 2011. The motion of kelp blades and the surface renewal model. *Limnol. Oceanogr.* **56**: 1453–1462, doi:10.4319/lo.2011.56.4.1453
- HURD, C., P. HARRISON, AND L. DRUEHL. 1996. Effect of seawater velocity on inorganic nitrogen uptake by morphologically distinct forms of *Macrocystis integrifolia* from wave-sheltered and exposed sites. *Mar. Biol.* **126**: 205–214, doi:10.1007/BF00347445
- , AND C. PILDITCH. 2011. Flow-induced morphological variations affect diffusion boundary-layer thickness of *Macrocystis pyrifera* (Heterokontophyta, Laminariales). *J. Phycol.* **47**: 341–351, doi:10.1111/j.1529-8817.2011.00958.x
- JACKELMAN, J., AND J. BOLTON. 1990. Form variation and productivity of an intertidal foliose *Gigartina* species (Rhodophyta) in relation to wave exposure. *Hydrobiologia* **204**: 57–64, doi:10.1007/BF00040215
- KOEHL, M., AND R. ALBERTE. 1988. Flow, flapping, and photosynthesis of *Nereocystis luetkeana*: A functional comparison of undulate and flat blade morphologies. *Mar. Biol.* **99**: 435–444, doi:10.1007/BF02112137

- , W. SILK, H. LIANG, AND L. MAHADEVAN. 2008. How kelp produce blade shapes suited to different flow regimes: A new wrinkle. *Integr. Comp. Biol.* **48**: 834–851, doi:10.1093/icb/ich069
- KREGTING, L., C. HURD, C. PILDITCH, AND C. STEVENS. 2008. The relative importance of water motion on nitrogen uptake by the subtidal macroalga *Adamsiella chauvinii* (Rhodophyta) in winter and summer. *J. Phycol.* **44**: 320–330, doi:10.1111/j.1529-8817.2008.00484.x
- LAU, J. 1981. Stiffness of corrugated plate. *J. Eng. Mech. Div.* **107**: 271–275.
- LEDWELL, J. 1984. The variation of the gas transfer coefficient with molecular diffusivity, p. 293–302. *In* W. Brutsaert and G. Jirka [eds.], *Gas transfer at water surfaces*. Reidel.
- MANELA, A., AND M. HOWE. 2009. The forced motion of a flag. *J. Fluid Mech.* **635**: 439–454, doi:10.1017/S0022112009007770
- MICHELIN, S., AND S. L. SMITH. 2009. Resonance and propulsion performance of a heaving flexible wing. *Phys. Fluids* **21**, doi:10.1063/1.3177356
- , ———, AND B. GLOVER. 2008. Vortex shedding model of a flapping flag. *J. Fluid Mech.* **617**: 1–10, doi:10.1017/S0022112008004321
- PARKE, M. 1948. Studies on British Laminariaceae. I. Growth in *Laminaria saccharina* (L.) Lamour. *J. Mar. Biol. Assoc. U. K.* **27**: 651–709, doi:10.1017/S0025315400056071
- PERALTA, G., F. BRUN, J. PÉREZ-LLORÉNS, AND T. BOUMA. 2006. Direct effects of current velocity on the growth, morphometry and architecture of seagrasses: A case study on *Zostera noltii*. *Mar. Ecol. Prog. Ser.* **327**: 135–142, doi:10.3354/meps327135
- REYNOLDS, O. 1874. On the extent and action of the heating surface for steam boilers. *Proc. Manchester Lit. Philos. Soc.* **14**: 163–166.
- ROBERSON, L., AND J. COYER. 2004. Variation in blade morphology of the kelp *Eisenia arboriea*: Incipient speciation due to local water motion? *Mar. Ecol. Prog. Ser.* **282**: 115–128, doi:10.3354/meps282115
- ROMINGER, J. 2014. Hydrodynamic and transport phenomena at the interface between flow and aquatic vegetation: From the forest to the blade scale. Ph.D. thesis, Massachusetts Institute of Technology.
- SCHLICHTING, H. 1962. *Boundary layer theory*, 4th ed. McGraw-Hill.
- SJOTUN, K., AND S. FREDERIKSEN. 1995. Growth allocation in *Laminaria hyperborea* (Laminariales, Phaeophyceae) in relation to age and wave exposure. *Mar. Ecol. Prog. Ser.* **126**: 213–222, doi:10.3354/meps126213
- STEVENS, C., AND C. HURD. 1997. Boundary-layers around bladed aquatic macrophytes. *Hydrobiologia* **346**: 119–128, doi:10.1023/A:1002914015683
- , ———, AND P. ISACHSEN. 2003. Modelling of diffusion boundary-layers in subtidal macroalgal canopies: The response to waves and currents. *Aquat. Sci.* **65**: 81–91, doi:10.1007/s000270300007
- THOMAS, F., AND M. ATKINSON. 1997. Ammonium uptake by coral reefs: Effects of water velocity and surface roughness on mass transfer. *Limnol. Oceanogr.* **42**: 81–88, doi:10.4319/lo.1997.42.1.0081
- WELTY, J., C. WICKS, R. WILSON, AND G. RORRER. 2001. *Fundamentals of momentum, heat, and mass transfer*, 4th ed. Wiley.
- WERNBERG, T., AND M. THOMSEN. 2005. The effect of wave exposure on the morphology of *Ecklonia radiata*. *Aquat. Bot.* **83**: 61–70, doi:10.1016/j.aquabot.2005.05.007
- ZHANG, J., S. CHILDRESS, A. LIBCHABER, AND M. SHELLEY. 2000. Flexible filaments in a flowing soap film as a model for one-dimensional flags in a two-dimensional wind. *Nature* **408**: 835–839, doi:10.1038/35048530

Associate editor: James J. Leichter

Received: 09 December 2013

Accepted: 02 July 2014

Amended: 25 August 2014